SCFT Study of Diblock Copolymer Melts in Electric Fields: Selective Stabilization of Orthorhombic Fddd Network Phase

Jonathan M. Martin,† Wei Li,‡ Kris T. Delaney,*,‡ and Glenn H. Fredrickson*,†

†*Department of Chemical Engineering, University of California, Santa Barbara, CA 93106, USA*

‡*Materials Research Laboratory, University of California, Santa Barbara, CA 93106, USA*

E-mail: kdelaney@mrl.ucsb.edu; ghf@mrl.ucsb.edu

Abstract

Using self-consistent field theory (SCFT), we explore the phase behavior of a diblock copolymer melt in an applied electric field, with different dielectric constants assigned to each monomer type. The electric field penalizes the interfaces between species domains that are not parallel to the field. Under the present mean-field approximation, lamellar and cylindrical structures reorient to align their interfaces with the electric field, such that these mesophases will have the same electrostatic free energy contribution as the mixed (disordered) state, and their relative stability will remain unchanged. In contrast, sphere and network phases do not have an axis of dielectric uniformity; consequently, the preferred orientation and morphological response of these phases must be determined numerically. We compute the phase diagram for a BCP melt in the presence of an applied electric field by comparing the free energy of each phase at its thermodynamically-preferred orientation relative to the electric field vector. We find that the stability regions of the sphere and network phases shrink with increasing field strength, in favor of the disordered, cylindrical, and lamellar phases. Moreover, the double gyroid network phase is more strongly disfavored than the orthorhombic Fddd network phase, such that the predicted region of stability for the Fddd phase is shifted to larger segregation strength (lower temperature).

Introduction

The self-assembly of block copolymers (BCPs) has been a long-standing subject of interest due to the emergence of periodically repeating ordered microphases with features on the nanometer length scale.[1] This behavior has made BCPs an attractive platform for industrial production of materials and devices requiring placement of small repeating structures,[2] including semiconductor devices,[3,4] nanoporous membranes,[5,6] and other tunable functional nanomaterials.[2,7]

The BCP phase behavior can be faithfully captured by a coarse-grained molecular model of continuous Gaussian chains combined with self-consistent field theory (SCFT). SCFT is a mean-field approach[8,9] that is particularly efficient for dense, high-molar-mass polymer melts. Although it fails to reproduce certain features near the order-disorder transition,[10] SCFT is highly reliable for assessing the stability of copolymer microphases at intermediate to strong segregation strengths.[9,11]

The expected (lowest free energy) structure of the simplest AB diblock copolymer system can be determined within the SCFT framework by specifying two system parameters: volume fraction of A monomers (f) and an effective segregation strength parameter (χN). The latter is the product of a Flory parameter (χ) and the diblock degree of polymerization (N), and is sensitive to the chemistry of the two constituent monomers, the temperature, and the molar mass of the BCP.[1,8] It is currently predicted by SCFT and experimentally confirmed that seven phases compete for relative stability in this two-dimensional parameter space: disordered (DIS), lamellar (LAM), hexagonal-packed cylinders (HEX), BCC spheres, FCC/HCP spheres, the gyroid Ia$\bar{3}$d cubic network phase (GYR), and the orthorhombic Fddd network phase (O^{70}).[8,12–18] Knowledge of SCFT phase diagrams for both simple and complex BCPs has provided powerful guidance for materials design, interrogation, and application.

Of continuing interest is the effect of an applied electric field ($\mathbf{E}_0$) on the ordered structure in a BCP system. The tendency for BCP microphase structures to elongate or align along the direction of an applied electric field[19,20] has attracted attention as a potential experimental or industrial technique for enhancing or controlling the self-assembly process. For example, leveraging this alignment effect has been identified as a strategy for overcoming surface-air and surface-surface interactions to produce novel, perforated nanomaterials in directed self-assembly (DSA) applications.[21] Electric fields have also been identified as a means of enhancing the kinetics of the BCP self-assembly process,[22] greatly increasing the throughput potential of an industrial DSA workflow. Some other methods for aligning microstructures during the self-assembly process include application of magnetic fields,[23–25] localized annealing using high-performance photonic devices,[26,27] and epitaxial prepatterning.[2]

The driving force for alignment of BCP microphases in an electric field is posited to be the dielectric inhomogeneity in phase-separated BCP systems; the introduction of an applied electric field breaks the rotational invariance of bulk ordered structures, preferentially acting upon interfaces for which $\mathbf{E}_0$ has a component out-of-plane.[28,29] This broken-symmetry effect permits BCP nanostructures to exhibit anisotropic dielectric properties, even when purely isotropic behavior is prescribed at the monomer length scale.[30] Within the SCFT framework, a simple extension can be made to include the effect of an applied electric field. The electrostatic property of the system is specified by an inhomogeneous macroscopic dielectric constant, obtained from a linear constitutive relation between prescribed monomer dielectric constants and local volume fractions.

This modified SCFT formalism is inspired by an earlier model, wherein nonelectrostatic contributions to the behavior of the BCP melt are represented by a Ginzburg-Landau (GL) free energy functional that depends on an inhomogeneous composition field; the composition-dependence of the dielectric constant then biases this free energy when electrostatics are introduced. Using this formalism, Andelman and collaborators identified an electric field-induced phase transition in lamella-forming BCP thin films[31] and later reported the role of ionic impurities in altering the magnitude of field necessary to induce such a transition.[32] The latter has also more recently been studied using a full SCFT representation.[33]

This linear mixing rule for describing dielectric behavior of a BCP melt was later implemented within a full SCFT formalism, including several papers by Matsen[34–36] that address the self-assembly of BCPs confined to a thin gap between two charged plates. Among other novel results, Matsen's work identifies electric fields as a promising methodology for manufacture of perforated thin films by reorienting ordered cylindrical or lamellar structures perpendicular to the confinement. Matsen's work further demonstrates the efficacy and extensibility of the present SCFT model as a procedure for identifying stability limits, kinetic pathways,[34] and other properties and phenomena of interest. The full SCFT formalism has been shown to agree with the simpler GL model in the weak segregation regime.[37]

In another set of studies,[38,39] Schick and collaborators performed similar investigations, considering in detail the thermodynamic character of electric field-induced phase transitions in dielectric BCP systems. They identified several stable phases that exist for a cylinder-forming thin-film system, arising from competition between surface-wetting energy and dielectric response.[39]

More recently, Zvelindovsky and collaborators combined the electrostatic formalism with a dynamical SCFT framework to investigate the kinetic pathways of electric field-induced phase transitions and structure reorientations.[40–44] In one study,[43] this group used a dynamical extension of the GL model employed by Andelman to simulate the large-scale time-dependent rearrangement of defective lamellar structures subjected to an electric field. In striking agreement with experimental observations,[45] their results identified two healing mechanisms, one arising from the reorientation of locally ordered grains and one a "nucleation and growth" pathway – corresponding to the growth of perfectly aligned regions, with associated migrating boundaries that overrun the misaligned grains – and illuminated the role of segregation strength in selecting between them. In a later study,[46] they also identified a third mechanism in their simulations, "selective disordering" – wherein misaligned grains will melt into a disordered state, before recrystallizing as the aligned microstructure – which has been observed in experiments.[47,48]

In the present study, we use the full SCFT model to compute the complete diblock phase diagram for a bulk melt subjected to an external electric field, including all seven phases found in the field free state.[17] The field and temperature are treated as constant, with the implied assumption that any heating due to the conductivity of the melt will be mitigated by thermostatting. We assume purely dielectric constituent segments, a uniform applied electric field, and equal statistical segment lengths. We extend a previously-derived variable-cell updating method,[49] which permits the simulation cell shape and size to evolve to a stress-free configuration in tandem with solving the mean-field equations. In doing so, this approach automatically computes the commensurate unit-cell configuration for each morphology considered, permitting the free energy comparisons necessary for constructing the phase diagram of equilibrium morphologies. We show that the systems considered possess an orientation-sensitive free energy penalty arising from dielectric contrast, as described by Schick,[29] which selectively disfavors mesostructures that do not have an interface-free axis to align along the electric field vector. We show that this phenomenon has the effect of deforming phase boundaries of the diblock copolymer phase diagram, and in particular, preferentially stabilizing the O^{70} network phase relative to the GYR network phase, permitting access to the former structure at larger values of χN for intermediate field strengths.

Methods

We employ a field theory model based on a coarse-grained description of an incompressible, monodisperse melt of n diblock copolymer chains, with a contact Flory-Huggins repulsion,

χ, between dissimilar chain segments.[9] We invoke the continuous Gaussian chain model and assume a locally isotropic dielectric response of the constituent segments. In the SCFT framework, this leads to an electric field-induced shift of the effective potential felt by a segment of species j (A or B):

$$w_j^{eff}(\mathbf{r}) = w_j(\mathbf{r}) - \frac{\beta \epsilon_j \varepsilon_0}{2N} |\nabla \psi(\mathbf{r})|^2, \tag{1}$$

where $w_j(\mathbf{r})$ is the auxiliary chemical potential field experienced by segments of type j due to non-electrostatic effects (immiscibility and incompressibility); its form is specified by the exchange field-theoretic formalism of Model E, described in Ref. 9. ε_0 is the vacuum permittivity, ϵ_j is the dielectric constant of type j segments, and $\psi(\mathbf{r})$ is the local electrostatic potential, such that $-\nabla\psi$ represents the local electric field experienced by a segment at position $\mathbf{r}$; the factor of N^{-1} ensures that the dielectric response of the melt is invariant to the length of the chains.

To determine the electric potential, we account for the heterogeneous dielectric response resulting from inhomogeneities in species densities and solve the differential form of Gauss' law in the absence of unbound charge:

$$\nabla \cdot [\epsilon(\mathbf{r}) \nabla \psi(\mathbf{r})] = 0 \tag{2}$$

where $\epsilon(\mathbf{r})$ is a dielectric profile, defined by a simple linear constitutive coupling to species densities:

$$\epsilon(\mathbf{r}) = \frac{1}{\rho_0} \sum_{j=A,B} \epsilon_j \tilde{\rho}_j \left(\mathbf{r}; \left[w_A^{eff}, w_B^{eff} \right] \right). \tag{3}$$

Here $\tilde{\rho}_j$ is the segment density operator for the jth segment species, presented in Eq. 16 in the Appendix. The imposed incompressibility condition requires a uniform total segment number density, ρ_0, at each position, $\mathbf{r}$, such that $\tilde{\rho}_A(\mathbf{r}) + \tilde{\rho}_B(\mathbf{r}) = \rho_0$. It was recently shown that this *ad hoc* model can be derived from a consistent microscopic origin by taking the incompressible, unsmeared (point dipole) limit of a general model of polarizable chain segments with self-consistently treated induced-dipoles on each segment.[50]

In addition to a shift in the effective potential field that alters the microphase free energies, the introduction of an applied electric field also induces morphological distortions of the phase structures. Consequently, some symmetries associated with the unperturbed candidate phase are broken, and equilibrium domain spacing becomes orientation-dependent. The unit cell shape and size must therefore be self-consistently optimized in the presence of the field to eliminate internal elastic stresses:

$$\tilde{\boldsymbol{\sigma}}[w_A^{eff}, w_B^{eff}, \mathbf{h}] = \mathbf{0}, \tag{4}$$

where $\tilde{\boldsymbol{\sigma}}$, defined in Eq. 18 in the Appendix, is the internal stress for a BCP melt subject to the effective chemical potential fields w_A^{eff} and w_B^{eff} within a periodically repeated arbitrary parallelepiped cell defined by the shape tensor $\mathbf{h}$.[49] For ease of notation, we retain the designations associated with the classical unperturbed morphologies, in contrast to other works, such as Ref. 51, wherein the authors define a distinct "ellipsoid" phase, corresponding to the reduced symmetry microstructure associated with a distorted BCC morphology.

Our SCFT procedure thus requires simultaneously relaxing the field configurations of the polymer melt (w_A, w_B) to the saddle-points specified in the exchange-mapped auxiliary field theory,[9,52] optimizing the shape and size of the periodic cell ($\mathbf{h}$) to a zero-stress configuration (Eq. 4) via the variable-cell method,[49] and determining the electric potential (ψ) self-consistently by solving Eq. 2 with appropriate boundary conditions. We solve the latter by enforcing periodic boundary conditions in the *local, internally-generated electric field*, $\mathbf{E}_{int} \equiv -\nabla\psi - \mathbf{E}_0$, and requiring $\int d\mathbf{r}\ \mathbf{E}_{int} = \mathbf{0}$, which is appropriate for a dielectric material. We note that although this condition is not sufficient to specify $\int d\mathbf{r}\ \psi$, it is sufficient to specify the local electric field, $-\nabla\psi$, which enters Eq. 1.

As discussed by Schick,[29] the introduction of an applied electric field to an inhomogeneous dielectric medium imparts an orientation sensitivity: configurations that violate the condition $\mathbf{E}_0 \cdot \nabla\epsilon = 0$ (*i.e.* that $\mathbf{E}_0$ is in the plane of any and all dielectric interfaces) will reduce the local electric field magnitude, resulting in a free energy penalty. It can be shown that this free energy penalty, which we define to be the difference in the electrostatic free energy for the inhomogeneous polymer melt and the corresponding term for the homogeneous (disordered) state with the same composition, is given by

$$\begin{aligned} \Delta F_{el} &= \frac{\varepsilon_0}{2}\int d\mathbf{r}\ \epsilon(\mathbf{r})\left[|\mathbf{E}_0|^2 - |\nabla\psi(\mathbf{r})|^2\right] \\ &= \frac{\varepsilon_0}{2}\int d\mathbf{r}\ \epsilon(\mathbf{r})|\mathbf{E}_{int}(\mathbf{r})|^2 \\ &= -\frac{\varepsilon_0}{2}\int d\mathbf{r}\ \psi_{int}(\mathbf{r})\left[\nabla\epsilon(\mathbf{r})\cdot\mathbf{E}_0\right], \end{aligned} \tag{5}$$

where ψ_{int} is the internally-generated contribution to the electric potential, defined by $-\nabla\psi_{int} = \mathbf{E}_{int}$. The form of the latter term of Eq. 5 emphasizes that ΔF_{el} vanishes when $\nabla\epsilon \cdot \mathbf{E}_0 = 0$. Consequently, we will find that the introduction of an applied electric field to a BCP melt induces elongation of ordered structures – and in some cases drives phase transitions to aligned structures – to reduce this free energy penalty.

In the weak segregation regime, the density profile for each monomer, $\tilde{\rho}_j$, is weakly inhomogeneous. Making the substitution $-\nabla\psi = -\nabla\psi_{int} + \mathbf{E}_0$ into Eq. 2, and solving the resulting PDE for ψ_{int} to leading order in the perturbation, $\Delta\rho = \tilde{\rho}_A - \rho_0 f$, the following asymptotic expression is obtained for the electrostatic free energy penalty,

$$\begin{aligned} \Delta F_{el} &\sim \frac{\kappa}{2}\int d\mathbf{r}\int d\mathbf{r}'\ \frac{\left(\nabla\tilde{\rho}_A(\mathbf{r})\cdot\mathbf{E}_0\right)\left(\nabla'\tilde{\rho}_A(\mathbf{r}')\cdot\mathbf{E}_0\right)}{\rho_0^2|\mathbf{r}-\mathbf{r}'|} \\ &\quad + O\left(\left[\frac{\Delta\rho}{\rho_0}\right]^3\right) \end{aligned} \tag{6}$$

$$\kappa \equiv \frac{\varepsilon_0(\epsilon_A - \epsilon_B)^2}{4\pi\bar{\epsilon}}, \tag{7}$$

where we have used the property, $\nabla\tilde{\rho}_A = -\nabla\tilde{\rho}_B$, which is required by incompressibility, and

$\bar{\epsilon}$ is the average macroscopic dielectric constant, defined as

$$\bar{\epsilon} \equiv \frac{1}{V} \int d\mathbf{r}\ \epsilon(\mathbf{r}) = \epsilon_A f + \epsilon_B (1 - f). \tag{8}$$

We note that Eq. 6 appears in numerous previous studies that employ this electrostatic formalism (*e.g.* Refs. 20,31), and is proportional to the square of the dielectric contrast between monomer species. Evidently, the dielectric response of a BCP melt in the weak segregation regime is specified by the single parameter, κ, such that the responses of systems with differing dielectric constant pairs may be collapsed to a common curve by a simple rescaling of $\mathbf{E}_0$. We therefore limit our calculations to a single pair of dielectric constants, with the understanding that the simulations must be repeated for other dielectric constant pairs when quantitative accuracy is required beyond the weak segregation regime.

Results and Discussion

Orientation Sensitivity in Dielectric Response

The orientation sensitivity imparted by an applied electric field has a symmetry-breaking property: for a fixed applied electric field, the free energy of a polymer mesostructure becomes sensitive to its orientation relative to the electric field vector, $\mathbf{E}_0$. In comparing free energies of competing phases, we choose the relative lattice orientation of a given mesostructure that minimizes its overall free energy response, as a bulk polymer melt can be expected to freely self-assemble in such a manner to attain this minimum in an applied electric field.

For the case of lamellae (LAM) and hexagonally packed cylinders (HEX), this optimal orientation is trivial to deduce:[29,53] each phase has at least one axis of dielectric uniformity, and can align such that the condition $\mathbf{E}_0 \cdot \nabla\epsilon = 0$ is everywhere satisfied – with the result that the free energy response, defined in Eq. 9 below, is 0. For structures without a uniform axis, this condition is not satisfied for any orientation of the microphase. The determination of the optimal orientation of the structure is thus made numerically while accounting for the self-consistent morphological response. Although this orientation sensitivity has been considered for the BCC phase,[53] it has yet to be explored in other 3D morphologies. The network phases shown to be stable by SCFT for a field-free diblock system, O^{70}[14] and GYR,[17] consist of complicated arrangements of species interfaces, and the preferred orientation of each mesostructure in a uniform applied electric field is not immediately obvious.

To interrogate the orientation-dependence of each network phase, a simple sweep was performed: the electric field magnitude was held constant, and the free energy response (Eq. 9) of the phase was calculated as a function of the relative orientation of the uniform applied electric field. The free energy response is defined to be

$$\Delta F(\theta, \phi) = F(\theta, \phi) - F_0 + \frac{\varepsilon_0 \bar{\epsilon} V}{2} |\mathbf{E}_0|^2 \tag{9}$$

where θ and ϕ specify the polar and azimuthal angles, respectively, of the orientation of the electric field vector on the unit sphere. $F(\theta, \phi)$ is the mean-field (SCFT) free energy of a given phase, subject to the applied electric field $\mathbf{E}_0$, F_0 is the free energy of each phase in the absence of an applied electric field, and the final term in Eq. 9 removes the dielectric response contribution to the free energy for a homogeneous mixed state.

In Fig. 1, we plot the intensive free energy response of the GYR and O^{70} phases in an electric field as a function of θ and ϕ. These results indicate that the GYR phase has a preferred (lowest free energy) electric field orientation of $\theta = \tan^{-1}\sqrt{2} \approx 0.955$, $\phi = \pi/4$, corresponding to the [111] direction, and the O^{70} phase has a preferred orientation of $\theta = 0$, which corresponds to the [001] direction.

The values on the scale bars for the contour plots in Fig. 1 show another important difference between the two structures: the free energy response varies little ($\sim$0.5%) as a function of electric field orientation for the GYR phase, whereas it changes by a factor of 5 for the O^{70} phase. Since the GYR phase belongs to a cubic crystal system, group-

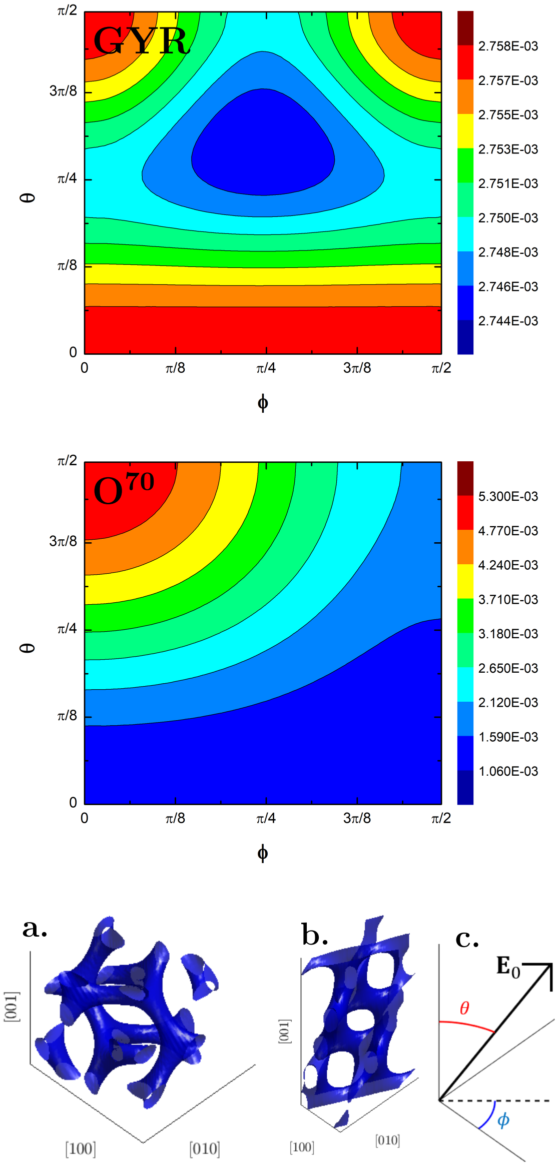

Figure 1: Intensive free energy response $[\beta\Delta F(\theta,\phi)/n]$ of GYR (top) and O^{70} (middle) phases at electric field strength $E_0[nkT/(\varepsilon_0 V)]^{-1/2} = 0.25$ for the diblock system of $f = 0.4$, $\chi N = 14.0$ and $\epsilon_A = 1.0$, $\epsilon_B = 4.0$. The images on the bottom row are 3D renders of the GYR (**a.**) and O^{70} (**b.**) unit cells and their corresponding lattice directions, along with a schematic (**c.**) depicting the correspondence between the angles (θ and ϕ) and the orientation of the field as applied to the two structures.

theoretic arguments demand that its linear response (*i.e.*, $E_0 \to 0$) be precisely isotropic,[54] and we can understand the weak anisotropy displayed in Fig. 1 as arising from the *nonlinear response* resulting from a *self-consistent* morphological distortion. On the other hand, the O^{70} phase is orthorhombic and admits a much stronger anisotropy in dielectric response that is finite in the linear response regime. One consequence of this anisotropy is that the free energy response of the O^{70} phase at its preferred orientation is smaller than that of GYR by $\sim 10^{-3} kT/n$, indicating a relative destabilization of the GYR phase.

To illuminate the scaling of this anisotropy effect, we compute the free energy for each network phase at two different electric field orientations, as a function of electric field magnitude, E_0, and plot the difference. We choose the [100] direction as an arbitrary direction that is disfavored for both phases and compare to the preferred orientation of each respective phase. The scaling identified in Fig. 2 indicates that the leading order term of this free energy difference varies as E_0^4 for the GYR phase and E_0^2 for the O^{70} phase. This indicates that the leading-order contribution to anisotropic dielectric response in the GYR phase must arise from nonlinear response, whereas the anisotropy of the O^{70} phase has a non-vanishing linear response contribution.

Diblock Phase Stability in an Applied Electric Field

We proceed by investigating the effect of the orientation-dependent dielectric response on the free energy competition that determines phase stability and order-order-transition boundaries. Fig. 3 shows the intensive SCFT free energy of GYR and each neighboring phase as a function of electric field magnitude, for values of f, χN at which GYR is most stable in the absence of a field. Since the free energy response is zero for both HEX and LAM in this SCFT framework, both network phases are eventually disfavored with sufficiently large electric fields. However, due to the stronger dielectric response of GYR over O^{70}, we also find a large window of electric field strengths within which the O^{70} phase is predicted to have the lowest free energy.

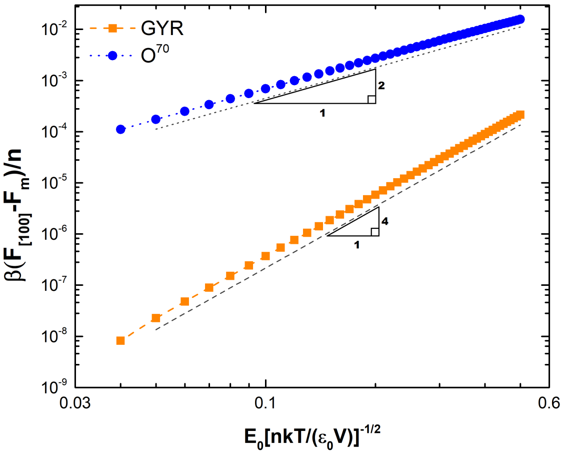

Figure 2: Difference in intensive free energy between two $\mathbf{E}_0$ orientations as a function of dimensionless field strength for the diblock system of $f = 0.4$, $\chi N = 14.0$ and $\epsilon_A = 1.0$, $\epsilon_B = 4.0$. The [100] direction is chosen for each phase as a disfavored orientation of $\mathbf{E}_0$, and the other is chosen to minimize the intensive free energy (F_m) for each corresponding phase structure. The dashed line has a slope of 4 and the dotted line has a slope of 2.

In Fig. 4, we plot the phase diagrams for diblock copolymer systems in the absence of an electric field (top) and in the presence of an electric field with dimensionless magnitude ($E_0 \left[nkT/(\varepsilon_0 V)\right]^{-1/2}$) of (middle) 0.25 and (bottom) 0.4. When an external electric field is introduced, the axially uniform LAM and HEX phases and the disordered phase are favored, such that the phase boundaries for both the order-disorder transitions (ODTs) and the order-order transitions (OOTs) shift to enlarge the stability regions corresponding to these structures.

The O^{70}-GYR phase boundary, which divides the network region of stability, is shifted by the electric field in favor of the O^{70} phase, a signature of the preferential destabilization of the GYR phase that was demonstrated in Fig. 3. To emphasize this shift, we also show an inset for the weak-segregation regime in the phase diagram with $E_0 \left[nkT/(\varepsilon_0 V)\right]^{-1/2} = 0.25$ in Fig. 4, third panel. This result may be of particular interest, since the O^{70} phase is predicted by SCFT to be thermodynamically stable only at weak segregation strength, and has only been obtained experimentally within a narrow temperature range.[16] Near the ODT, thermal fluctuations are expected to strongly perturb the phase diagram, and if sufficiently

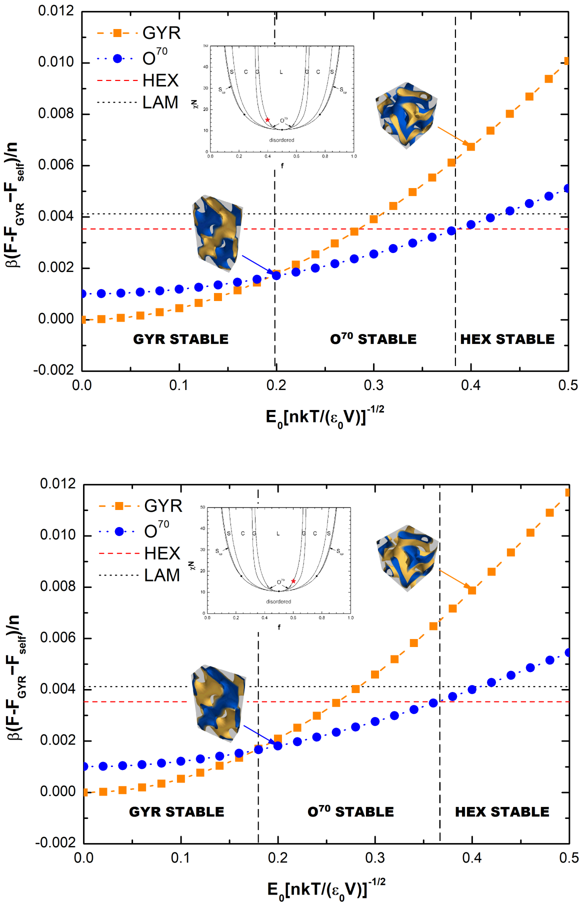

Figure 3: Free energy per molecule, $\beta F/n$, for the GYR and O^{70} phases, along with the HEX and LAM phases for reference, at their preferred orientations, as a function of dimensionless electric field strength, $E_0[nkT/(\varepsilon_0 V)]^{-1/2}$. The BCP parameters are $f = 0.4$ (top) and $f = 0.6$ (bottom), at $\chi N = 14.0$ and $\epsilon_A = 1.0$, $\epsilon_B = 4.0$. F_{GYR} is the free energy of the GYR phase in the absence of an applied electric field and $F_{self} = -(\bar{\epsilon}\varepsilon_0 V/2)E_0^2$ removes the bulk dielectric response of the mixed phase. The GYR phase is most stable at $E_0 = 0$, but there is an intermediate range of E_0 values for which O^{70} is favored.

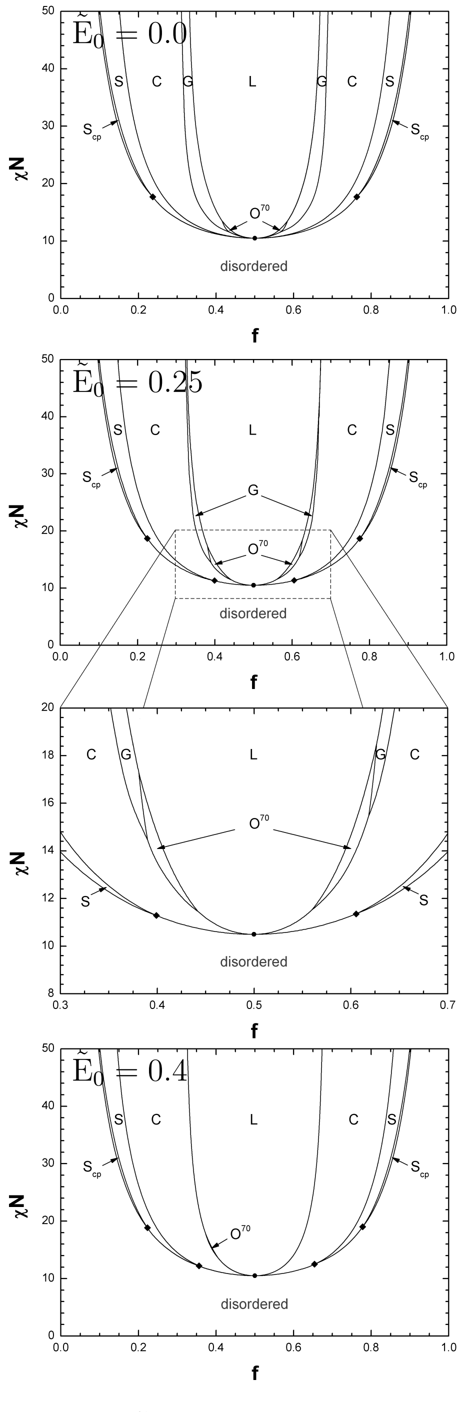

Figure 4: Diblock phase diagrams for $\tilde{\mathrm{E}}_0 \equiv E_0[nkT/(\varepsilon_0 V)]^{-1/2} = 0$ (top), 0.25 (middle two panels), and 0.4 (bottom), with $\epsilon_A = 1.0$, $\epsilon_B = 4.0$. The critical point (dot) is unaffected by the introduction of an applied electric field. However, the triple points (diamonds) shift to larger χN values and additional triple points emerge. The phase labels are: FCC spheres (S_{cp}), BCC spheres (S), hexagonal-packed cylinders (C), lamellar (L), $\mathrm{Ia\bar{3}d}$ double gyroid cubic network (G), and orthorhombic Fddd network (O^{70}).

strong, perhaps eliminate[55] the O^{70} region of thermodynamic stability when no electric field is present. The use of an electric field to shift the O^{70}-GYR phase boundary to larger segregation strengths may therefore prove to be a viable protocol for realizing the equilibrium stabilization of O^{70} at lower temperatures, where thermal fluctuations are weaker.

We note that in the present mean-field scheme, order-disorder transitions are also modified by the applied electric field if $f \neq 0.5$. However, the mean-field critical point lying at $f = 0.5$ is unaffected by the electric field due to the lack of dielectric response of both the LAM and DIS phases, in contrast with experimental predictions.[56] Evidently, a full treatment of composition fluctuations in tandem with an applied electric field is required to properly describe sensitivity of the ODT to applied fields.

At asymmetric ($f \neq 0.5$) compositions and in the absence of an electric field, SCFT predicts a narrow window of sphere-phase stability at the ODT. Under an applied electric field, DIS-HEX-BCC triple-points are predicted to appear; the electric field selectively destabilizes the BCC phase, so that there exists a segregation strength $\chi_{TP}N > \chi_c N$, where χ_{TP} is the triple point and χ_c is the critical point, below which the BCC phase is not thermodynamically stable. Below $\chi_{TP}N$, the ODT is predicted to be a first-order direct HEX-DIS transition. For the same reason, one can identify triple points (not marked on the phase diagram), delineating a χN window away from which direct LAM-HEX transitions emerge without intervening O^{70} or GYR phases.

Another important feature of the phase diagrams shown in Fig. 4 is the emergence of asymmetry about the vertical line passing through $f = 0.5$ (*i.e.* asymmetry in transposition of A and B monomer species) when an electric field is introduced. It can be seen that the previously discussed changes in the features of the phase diagram that emerge as a consequence of dielectric response (e.g. a narrower network phase window of stability) are more exaggerated on the large f side of the plot. For this side of the phase diagram, the B monomer (which we have selected to possess the larger dielectric constant of the two species) is the minority species, such that the average dielectric constant of a melt of this composition, $\bar{\epsilon}$, is smaller than for the composition corresponding to the opposing side of the phase diagram. As a consequence, the dielectric response of the melt, $\mathbf{E}_{int}$, is larger in magnitude, and the corresponding electrostatic free energy penalty, given by Eq. 5, is larger, consistent with the scaling predicted by the asymptotic form for ΔF_{el} derived in Eq. 6. This effect is also evident in Fig. 3, wherein the plot of free energy response at $f = 0.6$ indicates a stronger destabilization of the network phases, and the phase transitions from GYR to O^{70}, then from O^{70} to HEX, occur at smaller electric field magnitudes.

In designing an experiment that leverages the phase behavior of a BCP melt in an electric field, one would ideally want to choose an architecture for which the monomer species with the larger dielectric constant is the less abundant of the two. Doing so permits access to the desired effects with an electric field that is smaller in magnitude, reducing the demands of the experimental setup (*e.g.* a wider gap in a parallel-plate capacitor setup may be used) and reducing the risk that the strength of the field exceeds the dielectric breakdown limit of the monomer species.

Finally, we provide a rough estimate about the physical electric field strength by translating the dimensionless electric field strength $E_0[nkT/(\epsilon_0 V)]^{-1/2} = 0.25$ into a value in real units. We consider a BCP melt of intermediate chain concentration ($nR_g^3V^{-1} = 1.0$) and the radius of gyration $R_g = 10.0$ nm, operating in a parallel plate capacitor set-up at temperature $T = 200\,^{\circ}\mathrm{C}$. For such a system, the dimensionless electric field strength (specified in the middle phase diagram of Fig. 4) corresponds to a field strength of $E_0 = 6.79$ kV/mm, which is an order of magnitude below the dielectric breakdown strength of many common monomer chemistries and is well within physically realizable experimental values. This simple calculation supports the feasibility of applied electric fields as a modality for shifting phase boundaries and obtaining morphologies such as the O^{70} phase that might be otherwise difficult to access in bulk BCP systems.

Conclusion

We have presented a study of the equilibrium self-assembly of microphases of a BCP melt in the presence of a uniform applied electric field, $\mathbf{E}_0$. We assumed linear dielectric response in individual polymer chain segments and constructed a heterogeneous dielectric profile, ϵ, from a linear constitutive relation. The electrostatic potential is coupled to the melt configuration by self-consistently enforcing Gauss' law for an inhomogeneous dielectric (Eq. 2). Combining this constitutive model with existing field-theoretic methodology for simulating incompressible diblock copolymer melts, as well as a variable-cell relaxation method for automatically optimizing unit cell shape and size, we constructed the full mean-field diblock copolymer phase diagram, with prescribed species-dependent dielectric constants (ϵ_A, ϵ_B) and fixed electric field magnitude, E_0.

Our results show agreement with the qualitative predictions made by Schick,[29] as well as the results of other previous studies that employed the same linear constitutive model of inhomogeneous dielectric response. The free energy of an ordered phase structure in the presence of an electric field depends on its orientation relative to the electric field vector. This anisotropic dielectric response is present even for cubic phases (such as BCC and GYR phases) beyond the linear-response regime. The contrast in anisotropy between phases is subsequently responsible for the shift in phase transitions. One observation of particular interest is that the O^{70} network phase becomes relatively more thermodynamically stable than GYR as E_0 is increased, which shifts the GYR-O^{70} order-order transition to larger segregation strengths. As the O^{70} phase has been obtained experimentally[16] and predicted by simulation to exhibit marginal stability in the presence of sufficiently weak fluctuations,[55] we expect a window of stability to widen when a field of sufficient intensity is introduced, granting access to the O^{70} phase over a broader range of temperatures, chemistries, and molecular weights, and thus enhancing the materials design process when O^{70} is the desired microstructure.

The present results provide a prediction of the phase behavior of monocrystalline (*i.e.*

consisting of perfectly repeating unit cells) BCP melts. However, experimental and industrial setups are much larger than a single unit cell of a microphase, and imperfect long-range structures containing locally ordered grains of the appropriate microstructure (as in Ref. 43), or other defective states, exist as metastable melt configurations. In particular, the presence of a defect would have an orientation-sensitive – and highly case-dependent – effect on both the apparent OOT temperature associated with some desirable, field-induced transition (*e.g.* from GYR to O^{70}) and on the kinetics of this transition. However, we can make the assertion that there will be two general cases: 1) the defective structure remains metastable to the perfect crystal of the initial morphology upon introduction of an applied field, and 2) the defective structure becomes stable relative to the initial perfect structure in the presence of an applied field. In the former case, we predict little change to the OOT temperature or its kinetics, as we would expect the melt to recover the perfect initial morphology as an intermediate step, before a subsequent transition to the target structure, with the former transition having a much smaller free energy barrier, as it is simply a defect removal pathway. In the latter case, the OOT can be expected to shift in favor of the initial structure, as we are considering a defect that has a stabilizing effect in the presence of an electric field, delaying the onset of the OOT. The pathway for the eventual transition to the target structure would be distinct from that of the transition between two perfect morphologies; their relative free energy barriers would therefore need to be determined by experiment or simulation. Subsequent work in identifying these defective structures, their prevalence when a melt is quenched from the disordered state in the presence of an electric field, and the kinetic barriers associated with realignment of grains into a perfect microstructure – as well as other healing mechanisms – will therefore be of use to the experimentalist interested in using an applied electric field to obtain novel, defect-free morphologies. Additionally, the combination of applied electric fields with other techniques for enhancing the annealing process, such as the use of non-selective solvent,[57] requires further consideration; for example, one would expect to need a larger electric field to obtain a desired shift in phase behavior when a solvent is present, as the solvent's contribution to the dielectric character of the solution reduces the dielectric contrast between domains.

As described in Results, the LAM and HEX microphases possess an axis of dielectric uniformity, such that they may align their interfaces parallel to the electric field vector, their thermodynamic stability – relative to each other and to the DIS phase – is unchanged, and the sphere and network phases become selectively disfavored. Indeed, for sufficiently large electric fields, one could expect the sphere and network phases to be disfavored at all values of f and χN, such that the resulting diblock phase diagram consists of only DIS, HEX, and LAM regions of stability, with corresponding phase boundaries that are insensitive to further increases in electric field strength. As a consequence, our results predict no shift in the BCP critical point lying at $f = 0.5$. However, experiment confirms that the critical point for a BCP shifts to larger χN values (lower temperature) in response to an applied electric field.[56]

In an early study,[58] Debye and Kleboth measured a field-induced depression of the critical temperature of a binary small-molecule mixture. They also measured the composition dependence of the dielectric constant of the mixture, and observed a depression, relative to a linear mixing rule; inserting this composition dependence into the electrostatic free energy contribution, they obtained predictions for a field-induced shift that agreed quantitatively with their critical point measurements. Wirtz and Fuller later observed similar behavior in polymer solutions,[59] and we thus expect that a similar effect is also present in BCP systems. Evidently, the present non-fluctuating SCFT model, which assumes a linear mixing rule for the dielectric behavior of the melt, is insufficient to describe this qualitative behavior – we thus posit that this shift arises from fluctuation effects – in particular, that the composition fluctuations that give rise to microphase separation are selectively suppressed. We propose extension to a fully-fluctuating model for dielectric BCPs and other dielectric binary mixtures – as described in Ref. 50 – as a well-suited modality for investigating this phenomenon.

Beyond the simple isotropic polarizability prescribed in the present dielectric model, one may also introduce an anisotropic polarizability, which couples chain conformation to the local electric field, altering phase boundaries and domain spacing.[60,61] This effect is primarily only significant for systems containing stiff polymers in a magnetic field,[62] wherein an equation analogous to Gauss' law (Eq. 2) governs the diamagnetic response of the melt. For block copolymer systems composed of chemistries that are more strongly polarizable parallel to the chain backbone, and for which there is diamagnetic contrast between A and B monomer species, magnetostatic free energy contributions due to alignment of chains and to alignment of microstructure domains, respectively, compete; these types of physical systems thus exhibit a rich, orientation-sensitive phase behavior.[63]

Acknowledgement

JMM was supported by the Institute for Collaborative Biotechnologies through grant W911NF-09-D-0001-0042 from the U.S. Army Research Office. KTD and GHF were partially supported by the NSF DMR-CMMT Program under award DMR-1506008, and by the Institute for Collaborative Biotechnologies through grant W911NF-09-0001 from the U.S. Army Research Office. The content of the information presented here does not necessarily reflect the position or the policy of the U.S. Government, and no official endorsement shall be inferred. Extensive use was made of the computational facilities of the Center for Scientific Computing at the CNSI and MRL: an NSF MRSEC (DMR-1720256) and NSF CNS-1725797.

Appendix:

Single-chain statistics and stress operator

We seek to evaluate the internal stress operator, given by:

$$\begin{aligned}\tilde{\boldsymbol{\sigma}}[w_A^{eff}, w_B^{eff}, \mathbf{h}] &= -\frac{2nkT}{V}\mathbf{h}\frac{\partial \ln Q[w_A^{eff}, w_B^{eff}, \mathbf{g}]}{\partial \mathbf{g}}\mathbf{h}^T \\ &\quad -\varepsilon_0\bar{\epsilon}\mathbf{E}_0\mathbf{E}_0^T, \end{aligned} \tag{10}$$

where $\mathbf{A}^T$ denotes the transpose of a tensor $\mathbf{A}$ and $\mathbf{g} = \mathbf{h}^T\mathbf{h}$ is the metric tensor associated with the cell. The latter term in the above expression arises when we require that the mixed state admit no electrostatic stress response. The volume of the simulation cell is given by $V = \det \mathbf{h}$, and Q is the single-chain partition function, defined as

$$Q[w_A^{eff}, w_B^{eff}, \mathbf{g}] = \int d\mathbf{x}\, q(\mathbf{x}, 1) \tag{11}$$

with $\mathbf{x} \in [0,1]^3$ a cell-scaled coordinate, related to the dimensional position in space by $\mathbf{r} = \mathbf{h}\mathbf{x}$, and q a chain propagator object that solves the modified anisotropic diffusion equation

$$\begin{aligned}\frac{\partial}{\partial s}q(\mathbf{x}, s) &= \left[R_g^2\nabla_{\mathbf{x}}^T\mathbf{g}^{-1}\nabla_{\mathbf{x}} - W(\mathbf{x}, s)\right]q(\mathbf{x}, s) \\ q(\mathbf{x}, 0) &= 1 \qquad s \in [0,1]. \end{aligned} \tag{12}$$

The length-scale $R_g = b\sqrt{N/6}$ is the bare radius of gyration of a conformationally symmetric BCP with statistical segment length $b = b_A = b_B$, and N is the degree of polymerization. W gives the local field experienced by the segment at contour position s,

$$W(\mathbf{x}, s) = \begin{cases} W_A^{eff}(\mathbf{x}) & s < f \\ W_B^{eff}(\mathbf{x}) & s \geq f \end{cases}, \tag{13}$$

where the cell-scaled species fields are related to their dimensional counterparts by $W_j^{eff}(\mathbf{x}) = N w_j^{eff}(\mathbf{r})$.

Using a technique detailed by Villet *et al.*,[64] one may apply the derivative $\frac{\partial}{\partial \mathbf{g}}$ to Eq. 12 and arrive at a PDE that results in the following expression for the internal stress operator:

$$\tilde{\boldsymbol{\sigma}}\left[w_A^{eff}, w_B^{eff}, \mathbf{h}\right] = \frac{nkT}{V}\int d\mathbf{x}\left[\mathbf{h}\tilde{\boldsymbol{\Sigma}}(\mathbf{x})\mathbf{h}^T\right.$$
$$\left.+\sum_{j=A,B}\frac{\partial W_j^{eff}(\mathbf{x})}{\partial \mathbf{h}}\mathbf{h}^T\tilde{\phi}_j(\mathbf{x})\right] - \varepsilon_0\bar{\epsilon}\mathbf{E}_0\mathbf{E}_0^T. \tag{14}$$

$\tilde{\Sigma}$ can be interpreted as a local, cell-scaled, single-chain contribution to the internal stress and is given by

$$\tilde{\boldsymbol{\Sigma}}(\mathbf{x}) = \frac{2}{Q}\int_0^1 ds \quad q(\mathbf{x},s)\left(R_g^2\mathbf{g}^{-1}\nabla_{\mathbf{x}}\nabla_{\mathbf{x}}^T\mathbf{g}^{-1}\right)$$
$$\times q^\dagger(\mathbf{x},1-s), \tag{15}$$

where $q^\dagger$ is a complementary propagator, which solves Eq. 12, with $W(\mathbf{x},s)$ replaced by $W^\dagger(\mathbf{x},s) \equiv W(\mathbf{x},1-s)$. Similarly, $\tilde{\phi}_j$ is a cell-scaled volume fraction operator, defined as

$$\begin{aligned}\tilde{\phi}_j(\mathbf{x}) &= \frac{1}{Q}\int_0^1 ds\; u_j(s)q(\mathbf{x},s)q^\dagger(\mathbf{x},1-s)\\ &= \frac{1}{\rho_0}\tilde{\rho}_j\left(\mathbf{r};\left[w_A^{eff}, w_B^{eff}\right]\right)\end{aligned} \tag{16}$$

with u_j a function that selects the limits of integration according to the identity of the desired species, j:

$$u_j(s) = \begin{cases}\Theta(f-s) & j = A\\ \Theta(s-f) & j = B\end{cases}, \tag{17}$$

where Θ is the Heaviside function. The latter expression of Eq. 16 identifies the connection to the segment density operator described in Methods.

Substituting Eq. 1 into the expression for W_j^{eff} and noting that only the electrostatic term contributes a non-vanishing response to changes in the cell shape tensor, $\mathbf{h}$, we arrive at a final expression for the stress operator:

$$\tilde{\boldsymbol{\sigma}}\left[w_A^{eff}, w_B^{eff}, \mathbf{h}\right] = \frac{nkT}{V}\int d\mathbf{x}\ \mathbf{h}\tilde{\mathbf{\Sigma}}(\mathbf{x})\mathbf{h}^T + \tilde{\boldsymbol{\sigma}}_{el}[\psi], \tag{18}$$

where $\tilde{\boldsymbol{\sigma}}_{el}$ is an *electrostatic internal stress* contribution, given by:

$$\tilde{\boldsymbol{\sigma}}_{el}[\psi] = \frac{\varepsilon_0}{V}\int d\mathbf{r}\ \epsilon(\mathbf{r})\nabla\psi(\mathbf{r})\nabla^T\psi(\mathbf{r}) - \varepsilon_0\bar{\epsilon}\mathbf{E}_0\mathbf{E}_0^T. \tag{19}$$

References

(1) Bates, F. S.; Fredrickson, G. H. *Annual Review of Physical Chemistry* **1990**, *41*, 525–557.

(2) Trawick, M.; Angelescu, D.; Chaikin, P.; Register, R. In *Nanolithography and Patterning Techniques in Microelectronics*; Bucknall, D. G., Ed.; Taylor & Francis, 2005; Chapter 1, pp 1–38.

(3) Hamley, I. W. *Nanotechnology* **2003**, *14*, 39–54.

(4) Herr, D. J. C. *Journal of Materials Research* **2011**, *26*, 122–139.

(5) Hillmeyer, M. A. In *Block Copolymers II*; Abetz, V., Ed.; Springer Berlin Heidelberg, 2005; Chapter 3, pp 137–181.

(6) Jackson, E. A.; Hillmeyer, M. A. *ACS Nano* **2010**, *4*, 3548–3553.

(7) Kim, J. K.; Yang, S. Y.; Lee, Y.; Kim, Y. *Progress in Polymer Science* **2010**, *35*, 1325–1349.

(8) Matsen, M. W.; Schick, M. *Physical Review Letters* **1994**, *72*, 2660–2663.

(9) Fredrickson, G. H. *The Equilibrium Theory of Inhomogeneous Polymers*; Oxford University Press: New York, 2006.

(10) Fredrickson, G. H.; Helfand, E. *Journal of Chemical Physics* **1987**, *87*, 697–795.

(11) Matsen, M. W. *Journal of Physics: Condensed Matter* **2001**, *14*, R21.

(12) Bates, F. S.; Schulz, M. F.; Khandpur, A. K.; Forster, S.; Rosedale, J. H.; Almdal, K.; Mortensen, K. *Faraday Discuss.* **1994**, *98*, 7–18.

(13) Matsen, M. W.; Bates, F. S. *Macromolecules* **1996**, *29*, 1091–1098.

(14) Tyler, C. A.; Morse, D. C. *Physical Review Letters* **2005**, *94*, 208302.

(15) Yamada, K.; Nonomura, M.; Ohta, T. *Journal of Physics: Condensed Matter* **2006**, *18*, 421–427.

(16) Kim, M. I.; Wakada, T.; Akasaka, S.; Nishitsuji, S.; Saijo, K.; Hasegawa, H.; Ito, K.; Takenaka, M. *Macromolecules* **2008**, *41*, 7667–7670.

(17) Matsen, M. W. *Macromolecules* **2012**, *45*, 2161–2165.

(18) Li, W.; Delaney, K. T.; Fredrickson, G. H. *Journal of Polymer Science Part B: Polymer Physics* **2016**, *54*, 1112–1117.

(19) Amundson, K.; Helfand, E.; Davis, D. D.; Quan, X.; Patel, S. S.; Smith, S. D. *Macromolecules* **1991**, *24*, 6546–6548.

(20) Amundson, K.; Helfand, E.; Quan, X.; Smith, S. D. *Macromolecules* **1993**, *26*, 2698–2703.

(21) Darling, S. B. *Progress in Polymer Science* **2007**, *32*, 1152–1204.

(22) Jeon, H. U.; Jin, H. M.; Kim, J. Y.; Cha, S. K.; Mun, J. H.; Lee, K. E.; Oh, J. J.; Yun, T.; Kim, J. S.; Kim, S. O. *Molecular Systems Design & Engineering* **2017**, *2*, 560–566.

(23) Rokhlenko, Y.; Zhang, K.; Gopinadhan, M.; Larson, S. R.; Majewski, P. W.; Yager, K. G.; Gopalan, P.; O'Hern, C. S.; Osuji, C. O. *Physical Review Letters* **2015**, *115*, 258302.

(24) Gopinadhan, M.; Choo, Y.; Kawabata, K.; Kaufman, G.; Feng, X.; X. Di, Y. R.; Mahajan, L. H.; Ndaya, D.; Kasi, R. M.; Osuji, C. O. *Proceedings of the National Academy of Sciences* **2017**, *104*, E9437.

(25) Rokhlenko, Y.; Majewski, P. W.; Larson, S. R.; Gopalan, P.; Yager, K. G.; Osuji, C. O. *ACS Macro Letters* **2017**, *6*, 404–409.

(26) Jin, H. M.; Park, D. Y.; Jeong, S.; Lee, G. Y.; Kim, J. Y.; Mun, J. H.; Cha, S. K.; Lim, J.; Kim, J. S.; Kim, K. H.; Lee, K. J.; Kim, S. O. *Advanced Materials* **2017**, *29*, 1700595.

(27) Yong, D.; Jin, H. M.; Kim, S. O.; Kim, J. U. *Macromolecules* **2018**, *51*, 1418–1426.

(28) Liedel, C.; Pester, C. W.; Ruppel, M.; Urban, V. S.; Böker, A. *Macromolecular Chemistry and Physics* **2012**, *213*, 259–269.

(29) Schick, M. In *Polymers, Liquids, and Colloids in Electric Fields: Interfacial Instabilities, Orientation, and Phase Transitions*; Tsori, Y., Steiner, U., Eds.; World Scientific, 2009; Chapter 1, pp 197–214.

(30) Onuki, A.; Fukuda, J. *Macromolecules* **1995**, *28*, 8788–8795.

(31) Tsori, Y.; Andelman, D. *Macromolecules* **2002**, *35*, 5161–5170.

(32) Tsori, Y.; F.Tournilhac,; Andelman, D.; Leibler, L. *Physical Review Letters* **2003**, *90*, 145504.

(33) Dehghan, A.; Schick, M.; Shi, A. *Journal of Chemical Physics* **2015**, *143*, 134902.

(34) Matsen, M. W. *Physical Review Letters* **2005**, *95*, 258302.

(35) Matsen, M. W. *Macromolecules* **2006**, *39*, 5512–5520.

(36) Matsen, M. W. *Journal of Chemical Physics* **2006**, *124*, 074906.

(37) Tsori, Y.; Andelman, D.; Lin, C.; Schick, M. *Macromolecules* **2006**, *39*, 289–293.

(38) Lin, C.; Schick, M.; Andelman, D. *Macromolecules* **2005**, *38*, 5766–5773.

(39) Lin, C.; Schick, M. *Journal of Chemical Physics* **2006**, *125*, 034902.

(40) Ly, D. Q.; Honda, T.; Kawakatsu, T.; Zvelindovsky, A. V. *Macromolecules* **2007**, *40*, 2928–2935.

(41) Ly, D. Q.; Honda, T.; Kawakatsu, T.; Zvelindovsky, A. V. *Macromolecules* **2008**, *41*, 4501–4505.

(42) Ly, D. Q.; Honda, T.; Kawakatsu, T.; Zvelindovsky, A. V. *Soft Matter* **2009**, *5*, 4814–4822.

(43) Pinna, M.; Schreier, L.; Zvelindovsky, A. V. *Soft Matter* **2009**, *5*, 970–973.

(44) Ly, D. Q.; Pinna, M.; Honda, T.; Kawakatsu, T.; Zvelindovsky, A. V. *Journal of Chemical Physics* **2013**, *138*, 074904.

(45) Böker, A.; Elbs, H.; Hänsel, H.; Knoll, A.; Ludwigs, S.; Zettl, H.; Urban, V.; Abetz, V.; Müller, A. H. E.; Krausch, G. *Physical Review Letters* **2002**, *89*, 135502.

(46) Sevink, G. J. A.; Pinna, M.; Langer, K. M.; Zvelindovsky, A. V. *Soft Matter* **2011**, *7*, 5161–5170.

(47) Amundson, K.; Helfand, E.; Quan, X.; Hudson, S. D.; Smith, S. D. *Macromolecules* **1994**, *27*, 6559–6570.

(48) Ruppel, M.; Pester, C. W.; Langner, K. M.; Sevink, G. J. A.; Schoberth, H. G.; Schmidt, K.; Urban, V. S.; Mays, J. W.; Böker, A. *ACS Nano* **2013**, *7*, 3854–3867.

(49) Barrat, J.-L.; Fredrickson, G. H.; Sides, S. W. *Journal of Physical Chemistry B* **2005**, *109*, 6694–6700.

(50) Martin, J. M.; Li, W.; Delaney, K. T.; Fredrickson, G. H. *Journal of Chemical Physics* **2016**, *145*, 154104.

(51) Wu, J.; Wang, X.; Ji, Y.; He, L.; Li, S. *Physical Chemistry Chemical Physics* **2016**, *18*, 10309–10319.

(52) Düchs, D.; Delaney, K. T.; Fredrickson, G. H. *Journal of Chemical Physics* **2014**, *141*, 174103.

(53) Li, S.; Jiang, Y.; Ji, Y.; Wang, X. *Polymer* **2013**, *54*, 6636–6643.

(54) Nye, J. F. *Physical Properties of Crystals*; Clarendon Press, 1985.

(55) Delaney, K. T.; Fredrickson, G. H. *The Journal of Physical Chemistry B* **2016**, *120*, 7615–7634.

(56) Schoberth, H. G.; Pester, C. W.; Ruppel, M.; Urban, V. S.; Böker, A. *ACS Macro Letters* **2013**, *2*, 469–473.

(57) Böker, A.; Elbs, H.; Hänsel, H.; Knoll, A.; Ludwigs, S.; Zettl, H.; Zvelindovsky, A. V.; Sevink, G. J. A.; ; Urban, V.; Abetz, V.; Müller, A. H. E.; Krausch, G. *Macromolecules* **2003**, *36*, 8078–8087.

(58) Debye, P.; Kleboth, K. *Journal of Chemical Physics* **1965**, *42*, 3155.

(59) Wirtz, D.; Fuller, G. G. *Physical Review Letters* **1993**, *71*, 2236.

(60) Pester, C. W.; Ruppel, M.; Schoberth, H. G.; Schmidt, K.; Leidel, C.; van Rijn, P.; Schindler, K. A.; Hiltl, S.; Czubak, T.; Mays, J.; Urban, V. S.; Böker, A. *Advanced Materials* **2011**, *23*, 3999.

(61) Gurovich, E. *Macromolecules* **1994**, *27*, 7339–7362.

(62) Pester, C. W.; Liedel, C.; Ruppel, M.; Böker, A. *Progress in Polymer Science* **2017**, *64*, 182–214.

(63) Gopinadhan, M.; Choo, Y.; Osuji, C. O. *ACS Macro Letters* **2016**, *5*, 292–296.

(64) Villet, M. C.; Fredrickson, G. H. *Journal of Chemical Physics* **2014**, *141*, 224115.

For Table of Contents Only